

MutualForce: Mutual-Aware Enhancement for 4D Radar-LiDAR 3D Object Detection

Xiangyuan Peng^{*†} Huawei Sun^{*†} Kay Bierzynski[†] Anton Fischbacher^{*}
Lorenzo Servadei^{*} Robert Wille^{*}

^{*} Technical University of Munich, Munich, Germany

[†] Infineon Technologies AG, Neubiberg, Germany

Abstract—Radar and LiDAR have been widely used in autonomous driving as LiDAR provides rich structure information, and radar demonstrates high robustness under adverse weather. Recent studies highlight the effectiveness of fusing radar and LiDAR point clouds. However, challenges remain due to the modality misalignment and information loss during feature extractions. To address these issues, we propose a 4D radar-LiDAR framework to mutually enhance their representations. Initially, the indicative features from radar are utilized to guide both radar and LiDAR geometric feature learning. Subsequently, to mitigate their sparsity gap, the shape information from LiDAR is used to enrich radar BEV features. Extensive experiments on the View-of-Delft (VoD) dataset demonstrate our approach’s superiority over existing methods, achieving the highest mAP of 71.76% across the entire area and 86.36% within the driving corridor. Especially for cars, we improve the AP by 4.17% and 4.20% due to the strong indicative features and symmetric shapes.

Index Terms—3D object detection, Sensor fusion, Indicative feature, Shape information, Autonomous driving.

I. INTRODUCTION

Object detection is an important task in autonomous driving. Many detection algorithms have been developed based on various sensors, including cameras, LiDAR, and radar [1]–[4].

Cameras benefit from advanced 2D detection algorithms but lack depth perception and can raise privacy concerns [5]. In contrast, LiDAR point clouds provide detailed 3D geometric structures. Current LiDAR-based detection algorithms can be categorized into voxel-wise, point-wise, and hybrid-wise approaches. Voxel-wise methods partition point clouds into voxels or pillars [6], while point-wise methods extract features directly from raw points [7]. Some algorithms combine two methods to balance the computation cost and information loss [8]. However, the performance of LiDAR detection decreases over longer distances and is not robust in adverse conditions [9]. Small particles such as rain, fog, or dust can introduce noise to LiDAR point clouds [10], leading to false negative detections. Besides, LiDAR lacks velocity information, which is crucial for dynamic objects.

Consequently, radar has gained increased attention. Compared to LiDAR, radar remains robust performance over long distances and under extreme weather [11]–[13]. Besides, radar can reflect dynamic and material information by velocity and Radar Cross-Section (RCS) measurement. In particular, 4D radar additionally provides height information, contributing to

advancing radar-based detection in challenging environments [13]–[15]. However, 4D radar point clouds remain sparser compared to those from LiDAR, making it challenging to detect small and low-speed objects. Therefore, the practical application of radar-only detection is still limited.

To overcome the limitation of radar and LiDAR-only methods, a notable research direction is to fuse 4D radar and LiDAR point clouds [16]–[18], which combines accurate spatial information with high robustness. Some methods combine 4D radar and LiDAR points in the voxels or pillars, then use one joint encoder to extract united features [19], [20]. Other methods utilize two backbones to extract features parallelly and fuse them at the bird’s-eye view (BEV) stage [20]–[22]. However, most existing 4D radar-LiDAR fusion methods have not fully leveraged the unique strengths of each sensor to effectively interact with each other. The shortcomings can lead to information loss and misalignment between modalities. For example, radar provides velocity for dynamic objects, while RCS from radar is related to objects’ material, structure, and size. Integrating these radar-specific properties with the strong shape-aware LiDAR features can enhance the overall detection performance, especially for cars, which raise the most concern due to the special moving patterns and larger sizes.

Therefore, we propose a 4D radar-LiDAR fusion detection framework, MutualForce, that considers the advantages of both sensors and mutually enhances their own representations. First, velocity and RCS information from the radar are chosen as the indicative features, guiding both radar and LiDAR geometric feature extractions. Successively, a shape-awareness network at the BEV level enhances the radar’s BEV features using the shape information from LiDAR. The MutualForce outperforms existing methods on the View-of-Delft (VoD) dataset [14]. Overall, the main contributions are as follows:

- An Indicative Radar-Driven Bidirectional module (IRB), consisting of two branches, utilizes radar indicative information to guide geometric feature extraction of both radar and LiDAR point clouds.
- A multi-level Shape Awareness LiDAR-Driven Contrastive module (SALC) is introduced to enrich radar BEV features with LiDAR geometric information.
- Extensive experiments on the VoD dataset [14] demonstrate the effectiveness of our proposed method.

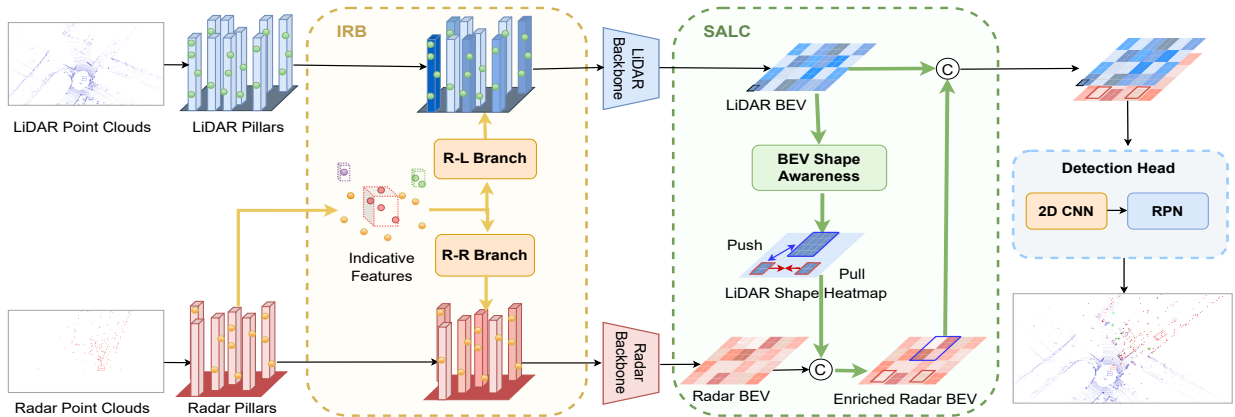


Fig. 1: The overall structure of MutualForce.

II. PROPOSED METHOD

A. Overall Structure

In this section, we introduce a fusion framework, MutualForce, which leverages the advantages of both sensors to mutually enhance their features. Its overall structure is illustrated in Fig. 1. Initially, radar and LiDAR point clouds are mapped into pillars. Later, in the IRB module, the radar indicative features guide both radar and LiDAR geometric feature learning through a bidirectional attention mechanism. Subsequently, the multi-level shape information from LiDAR enriches radar BEV features by the SALC module. The final radar and LiDAR BEV features are concatenated and fed into the detection head to generate 3D proposals.

B. Indicative Radar-Driven Bidirectional (IRB) Fusion

In open areas, compared to high-speed vehicles, cyclists and pedestrians often have lower speed ranges with varied movement patterns. To effectively distinguish different moving road users, utilizing both the radar relative radial velocity and absolute radial velocity after ego-motion compensation becomes necessary. However, in densely populated environments, there are more low-speed or stationary vehicles, as illustrated in Fig. 2(a). They may have similar velocities as cyclists or pedestrians. In such cases, RCS from radar provides supplementary information since it relates to the object's structure, material, and size [23]. As shown in Fig. 2(b), cars have metallic surfaces with distinct reflections compared to pedestrians and cyclists. Therefore, we choose the relative radial velocity, absolute radial velocity, and RCS from radar as the indicative features in the IRB module.

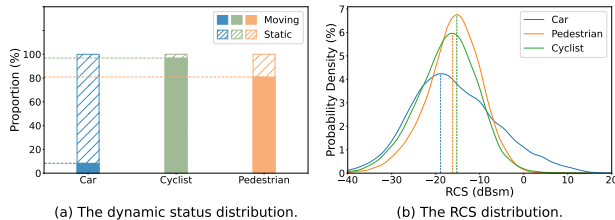


Fig. 2: The distribution of radar indicative features for different road users in the VoD dataset.

The structure of the IRB module is illustrated in Fig 3. It consists of two branches, R-R and R-L, guiding radar and LiDAR geometric feature learning. After the pillarization of

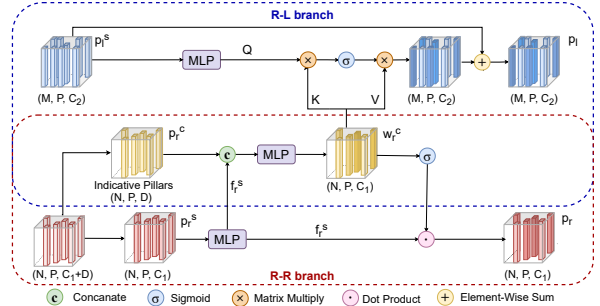


Fig. 3: The Structure of IRB module.

the raw point clouds, radar indicative pillars p_r^c and spatial pillars p_r^s have the dimension of (N, P, D) and (N, P, C_1) while LiDAR pillars p_l^s are in dimension (M, P, C_2) . M and N represent the number of pillars, P denotes the number of points in each pillar. C_1 and C_2 are the feature channels. $D = 3$ indicates the three chosen radar indicative features, relative and absolute radial velocity, and RCS.

In the R-R branch, the radar intermediate geometric feature f_r^s is first captured from p_r^s through a Multilayer Perceptron (MLP). Then the indicative feature p_r^c is concatenated with f_r^s to balance the indicative and geometric information and generate indicative weight w_r^c . Subsequently, the indicative weight guides the radar spatial feature through a Sigmoid function and dot-product operation. The process of generating the final radar feature p_r can be formulated as:

$$w_r^c = \text{MLP}(p_r^c \textcircled{C} f_r^s), \quad p_r = \sigma(w_r^c) \cdot f_r^s, \quad (1)$$

where \textcircled{C} denotes the concatenation. In the end, the radar representation is enhanced by R-R branch.

In the R-L branch, the final LiDAR feature p_l is generated by a cross-attention mechanism. The LiDAR feature p_l^s undergoes an MLP as the query embedding Q , while the indicative weight w_r^c serves as key K and value V , bringing radar indicative information to LiDAR pillars

$$p_l = p_l^s + \left(\frac{QK^T}{\sqrt{d_k}} \right) \cdot V, \quad (2)$$

where $\left(\frac{QK^T}{\sqrt{d_k}}\right)$ represents the dot-product attention, d_k is key vectors' dimension. The dense LiDAR points can lead to redundant exploration of the background. By introducing radar indicative features, we include the dynamic and material information into LiDAR pillars. Therefore, LiDAR pillars can better identify important regions and foreground objects.

C. Shape Awareness LiDAR-Driven Contrastive (SALC) Fusion

Radar points reflected from foreground objects often show extremely incomplete shapes [24]. In contrast, LiDAR provides clearer fine-grained observation. It is particularly beneficial for cars with relatively symmetric shapes. Therefore, we propose the SALC module to enrich radar BEV features through the scene-level and instance-level shape information learned from LiDAR BEV features, as shown in Fig 4.

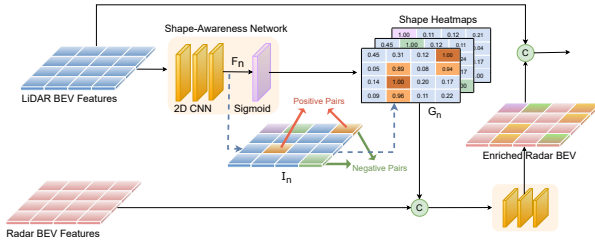


Fig. 4: The structure of SALC module.

In the SALC module, LiDAR BEV features $B \in \mathbb{R}^{H \times W \times C}$ from PointPillars backbones [25] are fed into a shape-awareness network composed of three 2D CNNs and one sigmoid layer. To obtain the global shape distribution, the shape-awareness network generates score-based shape heatmaps $G_n \in \mathbb{R}^{H \times W}$, $n = 1, \dots, N$, where N is the number of classes. Each grid in G_n indicates the likelihood of belonging to the shape of n -th class. A threshold τ is set to filter out the background grids. The remaining grids show the contours of the global scene. The awareness of scene-level shape distribution is supervised by the standard Focal Loss \mathcal{L}_{cls} [26].

Besides the scene-level shape distribution, instance-level understanding helps identify objects from different classes that show similar shapes due to occlusion and overlapping [27]. An efficient way of pushing away close objects from different classes is contrastive learning. Assuming $F_n = \{f(h, w) \mid h = 1, \dots, H, w = 1, \dots, W\}$ is the outputs before the sigmoid layer for the n -th class. According to CenterPoints [28], the grids in G_n with value 1 indicate the objects' centers. Therefore, N instance indicators I_n can be obtained by $I_n = \{f(h, w) \mid G_n(h, w) = 1\}$, $n = 1, \dots, N$. Leveraging the centers of instances, a "push and pull" strategy from Multi-class Contrastive (MCcont) Loss [29] is employed to separate close shapes from different classes. First, a matrix $S^{N \times M}$ is defined from I_n , where N denotes the number of classes, M is the maximum number of instance centers among all I_n . The elements in each row of S are the values in each I_n , indicating different instances from the same class. Columns of S are padded by randomly repeating the instances. S' is later obtained by swapping the columns of S . Elements in

the same row of S and S' are positive pairs from the same class, while elements in different rows are negative pairs. The instance-level contrastive shape separation is implemented as follows:

$$\mathcal{L}_{MCcont} = -\frac{1}{N} \sum_{h=1}^N \log \frac{\exp\left(\frac{d(S(h,:), S'(:,h))}{M^2}\right)}{\sum_{w \neq h} \exp\left(\frac{d(S(h,:), S'(:,w))}{M^2}\right)}, \quad (3)$$

where $d(\cdot, \cdot)$ denotes the distance calculated by element-wise product and sum. The shape-aware loss \mathcal{L}_{shape} is the sum of Focal Loss \mathcal{L}_{cls} [26] for foreground shape distribution and MCcont Loss \mathcal{L}_{MCcont} [29] for close instances separation:

$$\mathcal{L}_{shape} = \mathcal{L}_{cls} + \mathcal{L}_{MCcont}. \quad (4)$$

The generated shape heatmaps containing both global outline and instance details are integrated with radar BEV features via concatenation and convolution. Therefore, radar BEV features learn the multi-level shape information from LiDAR, supplementing missing and incomplete foreground geometric information. The enriched radar BEV features are concatenated with LiDAR BEV features to generate final proposals. Our network is trained by a standard Region Proposal Network (RPN) detection loss with the shape-aware loss,

$$\mathcal{L}_{final} = \mathcal{L}_{RPN} + \alpha \mathcal{L}_{shape}, \quad (5)$$

Here, α is set to 1.0.

III. EXPERIMENTS

In this section, we compared MutualForce with other 3D detection algorithms. The models were trained with 2 NVIDIA Tesla A30 GPUs for 80 epochs with a batch size of 8. The implementation was built upon OpenPCDet library [30].

A. Dataset and Metrics

Our approach is evaluated on the VoD dataset [14], containing 8600 frames of camera, LiDAR, and 4D radar data. Due to the unavailability of the test server, our evaluation is conducted on the validation set. We utilize the Average Precision (AP) for each class and the mean Average Precision (mAP) across all classes to evaluate the results. An IoU threshold of 50% is set for cars and 25% for cyclists and pedestrians. The performance is assessed in the entire area and the driving corridor.

B. Main Results

We performed extensive comparisons between MutualForce and existing single and multi-modal detection methods. The results are in Tables I. From Table I, radar-only and radar-camera methods yield unsatisfactory detection due to the sparsity of radar point clouds. In contrast, incorporating LiDAR significantly enhances the performance. Notably, our method outperforms other approaches with the mAP of 71.76% across the entire area and 86.36% in the driving corridor. Although most cars are static in the VoD dataset, as in Fig. 2(a), with the radar indicative information and LiDAR shape awareness, our method achieves an improvement of 4.17% and 4.20% AP for cars in two regions compared to Interfusion [16]. For small objects, our approach delivers better results, particularly in driving corridors, with a 1.99% AP increase for pedestrians

TABLE I: Comparative AP results on VoD val. set. The values are in %. The best results are bold.

Methods	Modality	All area				Driving Corridor			
		Car	Ped.	Cyc.	mAP	Car	Ped.	Cyc.	mAP
MVFAN [†] [31]	R	38.12	30.96	66.17	45.08	71.45	40.21	86.63	66.10
PV-RCNN [†] [8]	R	41.65	38.82	58.36	46.28	72.00	43.53	78.32	64.62
SMURF [32]	R	42.31	39.09	71.50	50.97	71.74	50.54	86.87	69.72
MUFASA [†] [33]	R	43.10	38.97	68.65	50.24	72.50	50.28	88.51	70.43
BEVFusion [34]	R+C	37.85	40.96	68.95	49.25	70.21	45.86	89.48	68.52
RCFusion [35]	R+C	41.70	38.95	68.31	49.65	71.87	47.50	88.33	69.23
RCBEVDet [36]	R+C	40.63	38.86	70.48	49.99	72.48	49.89	87.01	69.80
LXL [37]	R+C	42.33	49.48	77.12	56.31	72.18	58.30	88.31	72.93
Pointpillars [†] [25]	L	65.55	55.71	72.96	64.74	81.10	67.92	88.96	79.33
LXL-Pointpillars [37]	L	66.60	56.10	75.10	65.90	-	-	-	-
InterFusion [†] [16]	R+L	67.50	63.21	78.79	69.83	88.11	74.80	87.50	83.47
MutualForce (Ours)	R+L	71.67	66.26	77.35	71.76	92.31	76.79	89.97	86.36

R, C, and L denote the radar, camera, and LiDAR. [†] indicates our reproduced results.

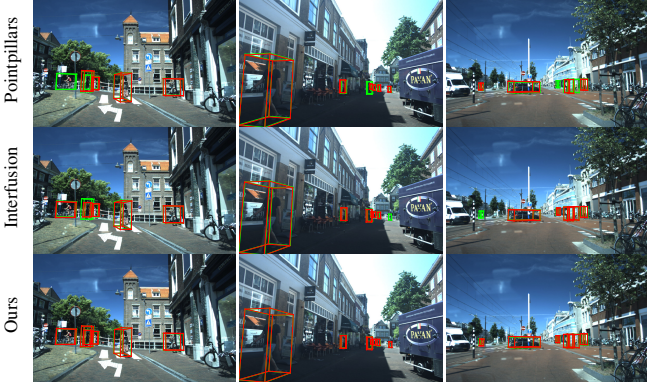


Fig. 5: Visualization of the detection on three methods. Ground truths are marked in green, while predicted boxes are red.

TABLE II: Analysis of each module. The values are in %.

IRB		SALC	All area				Driving Corridor			
R-R	R-L		Car	Ped.	Cyc.	mAP	Car	Ped.	Cyc.	mAP
✓			61.14	50.79	67.32	59.75	81.99	62.14	86.40	76.84
	✓		61.48	57.16	68.60	62.41	84.42	70.67	88.49	81.19
✓	✓		69.64	61.77	77.76	69.72	90.87	74.35	89.57	84.93
		✓	67.75	61.72	79.41	69.63	90.96	73.99	90.21	85.05
✓	✓	✓	69.53	59.58	74.77	67.96	90.74	72.69	88.81	84.08
		✓	71.67	66.26	77.35	71.76	92.31	76.79	89.97	86.36

and 2.47% for cyclists. Fig. 5 visualize the detection results of Pointpillars [25], Interfusion [16], and MutualForce. Our method performs better with fewer false negatives.

C. Ablation Study

Analysis of different modules: Experiments with different modules are presented in Table II. We first remove the IRB and SALC modules and directly concatenate two BEV features after feature extraction as the baseline. As shown in Table II, the R-L branch enhances the mAP by 9.97% and 8.09% in two regions, demonstrating that radar’s indicative information effectively guides LiDAR’s geometric features. Besides, the SALC module helps separate occluded objects by multi-level shape information, especially for cars and pedestrians, achieving an improvement of 8.39% and 8.79% in all areas.

Analysis of different indicative features: The ablation studies on different indicative features are in Table III. The baseline is implemented by removing the IRB module from the overall structure. According to Table III, velocity is important in detecting small objects. Leveraging relative and absolute

TABLE III: Analysis of indicative features. The values are %.

IRB			All area				Driving Corridor			
V_r	V_a	RCS	Car	Ped.	Cyc.	mAP	Car	Ped.	Cyc.	mAP
			69.53	59.58	74.77	67.96	90.74	72.69	88.81	84.08
✓			69.54	60.36	74.41	68.10	91.04	72.98	88.66	84.23
	✓		69.68	62.23	77.56	69.82	90.78	75.27	90.05	85.37
		✓	70.61	60.86	76.12	69.20	91.27	74.30	87.89	84.49
✓	✓		69.23	67.64	77.29	71.39	89.36	74.55	88.92	84.28
		✓	69.98	61.53	78.76	70.09	91.58	68.17	90.29	83.35
✓	✓	✓	69.34	67.08	77.14	71.19	91.43	74.53	88.31	84.76
✓	✓	✓	71.67	66.26	77.35	71.76	92.31	76.79	89.97	86.36

V_r denotes the relative radial velocity. V_a denotes the absolute radial velocity.

TABLE IV: Analysis of BEV threshold. The values are in %.

τ	All area				Driving Corridor			
	Car	Ped.	Cyc.	mAP	Car	Ped.	Cyc.	mAP
0.05	69.74	56.78	78.75	68.42	91.52	74.16	89.86	85.18
0.1	71.67	66.26	77.35	71.76	92.31	76.79	89.97	86.36
0.2	68.73	58.76	76.84	68.11	90.88	68.19	87.18	82.08

radial velocity improves the AP by 8.06% for pedestrians and 2.52% for cyclists in the entire scene. Besides, RCS enhances the detection due to the different surfaces’ materials.

Analysis of the BEV shape heatmaps in SALC: τ is used in SALC to determine whether a grid belongs to a shape. Results with different τ are in Table IV. Our model achieves the best mAP when τ equals 0.1, identifying the most shapes in LiDAR BEV features, especially for cars and pedestrians.

IV. CONCLUSION

Our MutualForce fully utilizes the respective strengths of radar and LiDAR to mutually enhance their representations. In the pillar stage, the radar’s indicative information guides the geometric feature extraction of both modalities. In the BEV stage, the multi-level shape information from LiDAR enriches the radar’s BEV features. Empirical evaluations on the VoD dataset demonstrate the superiority of our approach over existing single and multi-modal methods, achieving an improvement of mAP by 2.89% in the driving corridor. Besides, our model delivers a real-time performance at 14.45 FPS with 20.03M parameters.

ACKNOWLEDGMENT

This research was conducted as part of the DELPHI project, funded by the European Union under grant agreement No 101104263.

REFERENCES

- [1] Y. Peng, H. Li, Y. Zhang, X. Sun, and F. Wu, "Scene adaptive sparse transformer for event-based object detection," in *Proceedings of the IEEE/CVF Conference on Computer Vision and Pattern Recognition*, 2024, pp. 16 794–16 804.
- [2] F. Rollo, A. Zunino, N. Tsagarakis, E. M. Hoffman, and A. Ajoudani, "Carpe-id: Continuously adaptable re-identification for personalized robot assistance," *arXiv preprint arXiv:2310.19413*, 2023.
- [3] T. Rothmeier, W. Huber, and A. C. Knoll, "Time to shine: Fine-tuning object detection models with synthetic adverse weather images," in *Proceedings of the IEEE/CVF Winter Conference on Applications of Computer Vision*, 2024, pp. 4447–4456.
- [4] Y. Liu, M. Gehrig, N. Messikommer, M. Cannici, and D. Scaramuzza, "Revisiting token pruning for object detection and instance segmentation," in *Proceedings of the IEEE/CVF Winter Conference on Applications of Computer Vision*, 2024, pp. 2658–2668.
- [5] S. Zhao and S. Yan, "Bounding box-guided pseudo point clouds early-fusion and density optimize for 3d object detection," in *ICASSP 2024 - 2024 IEEE International Conference on Acoustics, Speech and Signal Processing (ICASSP)*, 2024, pp. 4205–4209.
- [6] X. Chen, S. Xu, X. Zou, T. Cao, D.-Y. Yeung, and L. Fang, "Svqnet: Sparse voxel-adjacent query network for 4d spatio-temporal lidar semantic segmentation," in *Proceedings of the IEEE/CVF International Conference on Computer Vision*, 2023, pp. 8569–8578.
- [7] K. Liu, Y. Zhu, Z. Wang, K. Wang, and G. Zhou, "Rethinking normals: Direction guided point cloud recognition," in *ICASSP 2024-2024 IEEE International Conference on Acoustics, Speech and Signal Processing (ICASSP)*. IEEE, 2024, pp. 8110–8114.
- [8] S. Shi, C. Guo, L. Jiang, Z. Wang, J. Shi, X. Wang, and H. Li, "Pv-rcnn: Point-voxel feature set abstraction for 3d object detection," in *Proceedings of the IEEE/CVF conference on computer vision and pattern recognition*, 2020, pp. 10 529–10 538.
- [9] Y. Chae, H. Kim, and K.-J. Yoon, "Towards robust 3d object detection with lidar and 4d radar fusion in various weather conditions," in *Proceedings of the IEEE/CVF Conference on Computer Vision and Pattern Recognition*, 2024, pp. 15 162–15 172.
- [10] M. Hahner, C. Sakaridis, D. Dai, and L. Van Gool, "Fog simulation on real lidar point clouds for 3d object detection in adverse weather," in *Proceedings of the IEEE/CVF International Conference on Computer Vision*, 2021, pp. 15 283–15 292.
- [11] D.-H. Paek, S.-H. Kong, and K. T. Wijaya, "K-radar: 4d radar object detection for autonomous driving in various weather conditions," *Advances in Neural Information Processing Systems*, vol. 35, pp. 3819–3829, 2022.
- [12] L. Saini, Y. Su, H. Tercan, and T. Meisen, "Centerpoint transformer for bev object detection with automotive radar," in *Proceedings of the IEEE/CVF Conference on Computer Vision and Pattern Recognition (CVPR) Workshops*, June 2024, pp. 4451–4460.
- [13] X. Zhang, L. Wang, J. Chen, C. Fang, L. Yang, Z. Song, G. Yang, Y. Wang, X. Zhang, and J. Li, "Dual radar: A multi-modal dataset with dual 4d radar for autonomous driving," *arXiv preprint arXiv:2310.07602*, 2023.
- [14] A. Palffy, E. Pool, S. Baratam, J. F. Kooij, and D. M. Gavrila, "Multi-class road user detection with 3+ 1d radar in the view-of-delft dataset," *IEEE Robotics and Automation Letters*, vol. 7, no. 2, pp. 4961–4968, 2022.
- [15] L. Zheng, Z. Ma, X. Zhu, B. Tan, S. Li, K. Long, W. Sun, S. Chen, L. Zhang, M. Wan *et al.*, "Tj4dradset: A 4d radar dataset for autonomous driving," in *2022 IEEE 25th International Conference on Intelligent Transportation Systems (ITSC)*. IEEE, 2022, pp. 493–498.
- [16] L. Wang, X. Zhang, B. Xv, J. Zhang, R. Fu, X. Wang, L. Zhu, H. Ren, P. Lu, J. Li *et al.*, "Interfusion: Interaction-based 4d radar and lidar fusion for 3d object detection," in *2022 IEEE/RSJ International Conference on Intelligent Robots and Systems (IROS)*. IEEE, 2022, pp. 12 247–12 253.
- [17] I. Roldan, A. Palffy, J. F. Kooij, D. M. Gavrila, F. Fioranelli, and A. Yarovoy, "See further than cfar: a data-driven radar detector trained by lidar," in *2024 IEEE Radar Conference (RadarConf24)*. IEEE, 2024, pp. 1–6.
- [18] Z. Meng, Y. Song, Y. Zhang, Y. Nan, and Z. Bai, "Traffic object detection for autonomous driving fusing lidar and pseudo 4d-radar under bird's-eye-view," *IEEE Transactions on Intelligent Transportation Systems*, 2024.
- [19] J. Song, L. Zhao, and K. A. Skinner, "Lirafusion: Deep adaptive lidar-radar fusion for 3d object detection," *arXiv preprint arXiv:2402.11735*, 2024.
- [20] Y. Wang, J. Deng, Y. Li, J. Hu, C. Liu, Y. Zhang, J. Ji, W. Ouyang, and Y. Zhang, "Bi-lrfusion: Bi-directional lidar-radar fusion for 3d dynamic object detection," in *Proceedings of the IEEE/CVF Conference on Computer Vision and Pattern Recognition*, 2023, pp. 13 394–13 403.
- [21] Y. Yang, J. Liu, T. Huang, Q.-L. Han, G. Ma, and B. Zhu, "Ralibev: Radar and lidar bev fusion learning for anchor box free object detection system," *arXiv preprint arXiv:2211.06108*, 2022.
- [22] K. Qian, S. Zhu, X. Zhang, and L. E. Li, "Robust multimodal vehicle detection in foggy weather using complementary lidar and radar signals," in *2021 IEEE/CVF Conference on Computer Vision and Pattern Recognition (CVPR)*, 2021, pp. 444–453.
- [23] S. Pang, Y. Zeng, H. Wang, Q. Yang, and B. Deng, "The rcs scaled measurement and inversion method for metal targets with rough surfaces based on the distribution of surface elements in the thz band," *IEEE Transactions on Antennas and Propagation*, 2024.
- [24] G. Peng, H. Li, Y. Zhao, J. Zhang, Z. Wu, P. Zheng, and D. Wang, "Transloc4d: Transformer-based 4d radar place recognition," in *Proceedings of the IEEE/CVF Conference on Computer Vision and Pattern Recognition*, 2024, pp. 17 595–17 605.
- [25] A. H. Lang, S. Vora, H. Caesar, L. Zhou, J. Yang, and O. Beijbom, "Pointpillars: Fast encoders for object detection from point clouds," in *Proceedings of the IEEE/CVF conference on computer vision and pattern recognition*, 2019, pp. 12 697–12 705.
- [26] T.-Y. Lin, P. Goyal, R. Girshick, K. He, and P. Dollár, "Focal loss for dense object detection," in *Proceedings of the IEEE international conference on computer vision*, 2017, pp. 2980–2988.
- [27] Y. Shen, Y. Zhang, Y. Wu, Z. Wang, L. Yang, S. Coleman, and D. Kerr, "Bsh-det3d: improving 3d object detection with bev shape heatmap," in *2023 IEEE/RSJ International Conference on Intelligent Robots and Systems (IROS)*. IEEE, 2023, pp. 5730–5737.
- [28] T. Yin, X. Zhou, and P. Krahenbuhl, "Center-based 3d object detection and tracking," in *Proceedings of the IEEE/CVF conference on computer vision and pattern recognition*, 2021, pp. 11 784–11 793.
- [29] Q. Xia, J. Deng, C. Wen, H. Wu, S. Shi, X. Li, and C. Wang, "Coin: Contrastive instance feature mining for outdoor 3d object detection with very limited annotations," in *Proceedings of the IEEE/CVF International Conference on Computer Vision*, 2023, pp. 6254–6263.
- [30] O. Team *et al.*, "Openpcdet: An open-source toolbox for 3d object detection from point clouds," *OD Team*, 2020.
- [31] Q. Yan and Y. Wang, "Mvfan: Multi-view feature assisted network for 4d radar object detection," in *International Conference on Neural Information Processing*. Springer, 2023, pp. 493–511.
- [32] J. Liu, Q. Zhao, W. Xiong, T. Huang, Q.-L. Han, and B. Zhu, "Smurf: Spatial multi-representation fusion for 3d object detection with 4d imaging radar," *IEEE Transactions on Intelligent Vehicles*, vol. 9, no. 1, pp. 799–812, 2024.
- [33] X. Peng, M. Tang, H. Sun, K. Bierzynski, L. Servadei, and R. Wille, "Mufasa: Multi-view fusion and adaptation network with spatial awareness for radar object detection," 2024. [Online]. Available: <https://arxiv.org/abs/2408.00565>
- [34] Z. Liu, H. Tang, A. Amini, X. Yang, H. Mao, D. L. Rus, and S. Han, "Bevfusion: Multi-task multi-sensor fusion with unified bird's-eye view representation," in *2023 IEEE International Conference on Robotics and Automation (ICRA)*, 2023, pp. 2774–2781.
- [35] L. Zheng, S. Li, B. Tan, L. Yang, S. Chen, L. Huang, J. Bai, X. Zhu, and Z. Ma, "Rcfusion: Fusing 4d radar and camera with bird's-eye view features for 3d object detection," *IEEE Transactions on Instrumentation and Measurement*, 2023.
- [36] Z. Lin, Z. Liu, Z. Xia, X. Wang, Y. Wang, S. Qi, Y. Dong, N. Dong, L. Zhang, and C. Zhu, "Rcbvdt: Radar-camera fusion in bird's eye view for 3d object detection," in *Proceedings of the IEEE/CVF Conference on Computer Vision and Pattern Recognition*, 2024, pp. 14 928–14 937.
- [37] W. Xiong, J. Liu, T. Huang, Q.-L. Han, Y. Xia, and B. Zhu, "Lxl: Lidar excluded lean 3d object detection with 4d imaging radar and camera fusion," *IEEE Transactions on Intelligent Vehicles*, 2023.